Intrinsically stretchable electrode array enabled in vivo electrophysiological mapping of atrial fibrillation at cellular resolution

Jia Liu[a,1], Xinyuan Zhang[b,c,1], Yuxin Liu[d,1], Miguel Rodrigo[c], Patrick D. Loftus[b], Joy Aparicio-Valenzuela[b], Jukuan Zheng[a], Terrence Pong[b], Kevin J. Cyr[b], Meghedi Babakhanian[c], Jasmine Hasi[e], Jinxing Li[a], Yuanwen Jiang[a], Christopher J. Kenney[e], Paul J. Wang[c], Anson M. Lee[b,2], and Zhenan Bao[a,2]

[a]Department of Chemical Engineering, Stanford University, Stanford, CA 94305; [b]Department of Cardiothoracic Surgery, School of Medicine, Stanford University, Stanford, CA 94305; [c]Division of Cardiovascular Medicine, Department of Medicine, School of Medicine, Stanford University, Stanford, CA 94305; [d]Department of Bioengineering, Stanford University, Stanford, CA 94305; and [e]SLAC National Accelerator Laboratory, Menlo Park, CA 94025

Edited by John A. Rogers, Northwestern University, Evanston, IL, and approved May 12, 2020 (received for review January 9, 2020)

Electrophysiological mapping of chronic atrial fibrillation (AF) at high throughput and high resolution is critical for understanding its underlying mechanism and guiding definitive treatment such as cardiac ablation, but current electrophysiological tools are limited by either low spatial resolution or electromechanical uncoupling of the beating heart. To overcome this limitation, we herein introduce a scalable method for fabricating a tissue-like, high-density, fully elastic electrode (elastrode) array capable of achieving real-time, stable, cellular level-resolution electrophysiological mapping in vivo. Testing with acute rabbit and porcine models, the device is proven to have robust and intimate tissue coupling while maintaining its chemical, mechanical, and electrical properties during the cardiac cycle. The elastrode array records epicardial atrial signals with comparable efficacy to currently available endocardial-mapping techniques but with 2 times higher atrial-to-ventricular signal ratio and >100 times higher spatial resolution and can reliably identify electrical local heterogeneity within an area of simultaneously identified rotor-like electrical patterns in a porcine model of chronic AF.

stretchable bioelectronics | in vivo cardiac mapping | high-density electrophysiology | atrial fibrillation

Atrial fibrillation (AF) is the most prevalent sustained arrhythmia in the United States, affecting more than 2.2 million people (1). The definitive treatment for symptomatic AF is cardiac ablation to restore sinus rhythm, although the success of this invasive treatment is suboptimal. During this procedure, an electrical-contact mapping catheter is navigated into the chambers of the heart and used to identify the regions that are responsible for the initiation and maintenance of the arrhythmia. Once these regions are identified, an ablation catheter is utilized to ablate the area through delivery of radiofrequency or cryothermal energy. Currently, the majority of clinical electroanatomic mapping is conducted in electrophysiology laboratories where endovascular electrodes are maneuvered under fluoroscopic guidance (2–5). However, these catheters are limited by low spatial resolution and an inability to map the epicardial surface of the heart (6). The limited resolution of current electrode catheters dictates the need for heavy reliance on postprocessing algorithms to reconstruct and identify arrhythmogenic regions. The identification of stable electrical rotors and focal discharged regions have been proposed as drivers of AF (6, 7), but the assumptions required to identify these drivers and the accuracy of such computed observations remain controversial (8). Moreover, high-resolution contact epicardial-mapping systems did not find as many stable drivers in one study (9). As a result, there is still a lack of understanding regarding the mechanisms of AF, particularly in the individual patient, which directly limits the efficacy of current therapies. New tools and methodologies are needed to effectively map the electrical activity of the heart in high resolution. These tools can provide insights into the underlying mechanisms driving AF and in turn provide effective and patient-specific ablation interventions.

We reasoned that this challenge could be addressed through high-density direct-contact mapping with the goal of achieving cellular-level resolution in a clinical set-up (10, 11). Recently, researchers have developed flexible thin-film electronics that directly contact heart tissue to offer improved electroanatomic mapping of the myocardium (12–14). However, due to the inelastic nature of the electronics, delamination from the myocardial surface can occur over the course of the dynamic cardiac cycle. To accommodate for the repeated displacement of the heart, serpentine metal interconnections (15–19) have been used to introduce elasticity in thin-film electronics. However, the serpentine structure limits the electrode-to-electrode distance. Furthermore, this technique has only been applied ex vivo in a rabbit model. To achieve cellular-level resolution, optical-mapping techniques using voltage-sensitive dyes have been employed previously for characterizing cardiac activation in ex vivo animal models (20–22). Unfortunately, optical mapping is not suitable for

Significance

Electrophysiological mapping of chronic atrial fibrillation (AF) at high throughput and high resolution is critical for understanding its underlying mechanism and guiding definitive treatment such as cardiac ablation, but current electrophysiological tools are limited by either low spatial resolution or electromechanical uncoupling of the beating heart. We herein introduce a microfabricated high-density, fully elastic electrode (termed elastrode) array for complex electrophysiological signal recording in vivo. We demonstrated the capability to identify clinically relevant electrophysiological heterogeneity in the pathologic state of pacing-induced chronic AF that was captured and correlated with state-of-the-art clinical techniques, which show the potential to apply this elastrode array toward elucidating the mechanism of AF at a cellular level and developing targeted AF therapy.

Author contributions: J. Liu, X.Z., Y.L., A.M.L., and Z.B. designed research; J. Liu, X.Z., Y.L., P.D.L., J.A.-V., J.Z., M.B., J.H., J. Li, Y.J., and C.J.K. performed research; J. Liu, X.Z., Y.L., M.R., K.J.C., P.J.W., A.M.L., and Z.B. analyzed data; and J. Liu, X.Z., T.P., A.M.L., and Z.B. wrote the paper.

The authors declare no competing interest.

This article is a PNAS Direct Submission.

[1]J. Liu., X.Z., and Y.L. contributed equally to this work.

[2]To whom correspondence may be addressed. Email: ansonlee@stanford.edu or zbao@stanford.edu.

This article contains supporting information online at https://www.pnas.org/lookup/suppl/doi:10.1073/pnas.2000207117/-/DCSupplemental.

First published June 15, 2020.

clinical use due to the potential toxicity of voltage-sensitive dyes and the challenge of removing image blurring from the mechanical movement of the heart (23). We envision that the incorporation of intrinsically stretchable polymeric electronic materials (24–26) into the cardiac electronics could offer a solution for high-density, high-resolution mapping without the need for serpentine designs or cellular-level manipulation. Currently, this remains a challenge due to the lack of photolithographic micropatterning methods for fully integrated elastic electrodes in the micrometer resolution.

Here, we introduce chemically orthogonal elastic electronic materials to enable micropatterning of a fully encapsulated and elastic electrode (elastrode). In the current work, we show the method for photolithographic microfabrication and assembly of wafer-scale elastrode array over 100 cm^2 that are suitable for mapping of large atrial surfaces. We applied this electrode array to the atrium in a porcine model of chronic AF, aiming to identify the pathological regions with high spatiotemporal resolution (Fig. 1*A*). We demonstrated that our fabricated elastrode array is able to 1) provide enhanced atrial signal recording due to the close contact to the heart tissue; 2) perform high-density mapping, capturing cellular-level electrophysiological heterogeneity in a porcine model of chronically stable AF; and 3) correlate high-density epicardial heterogeneous electrical patterns to conventional endocardial mapping results.

Results

Fabrication and Assembly of High-Density Elastrode Array. The major hurdles for adapting conventional photolithographic patterning processes on intrinsically stretchable polymers are due to their porous network, which readily swell in the presence of organic solvents used during the solution-based process. In our recent studies (24–26), we reported an intrinsically stretchable and tissue-level soft Au/poly(3,4-ethylenedioxy-thiophene):poly(styrene sulfonate) (PEDOT:PSS) conducting hydrogel, serving as stretchable electrodes and interconnections, and a chemically orthogonal, diacrylate-modified perfluoropolyether (PFPE-DMA) dielectric elastomer, serving as the stretchable insulation layer. Notably, a fluorinated solvent is used for processing and developing the PFPE-DMA patterns, compatible with most stretchable polymer materials and photoresists (*SI Appendix*, Fig. S1). By combining these two materials, here, we report a fabrication process to pattern a high-density, stretchable electrode array on a 4-inch wafer at sub-100-μm resolution. The multilayered, fully stretchable material patterning and assembly technique allows for creation of an elastrode array with spatially defined exposed electrode regions and interconnection lines protected by the stretchable PFPE-DMA passivation layer (Fig. 1*B*). Importantly, the use of photolithographic patterning allows for electrode sizes of less than 100 μm, comparable to the size of a single cardiomyocyte. Moreover, this technology can tightly cluster individual sensors in an unprecedented high-density package (64 electrical sensors in 0.25-cm^2 area), while still maintaining stretchability across the entire sensor array.

The elastrode array is fabricated on a rigid substrate with a dextran-based sacrificial layer that can be subsequently dissolved in water (Fig. 1 *C*, *I*). First, a layer of polydimethylsiloxane (PDMS) followed by a layer of PFPE-DMA are sequentially coated and cured as the bottom supporting layer and protective layer, respectively. The stretchable conductive PEDOT:PSS is

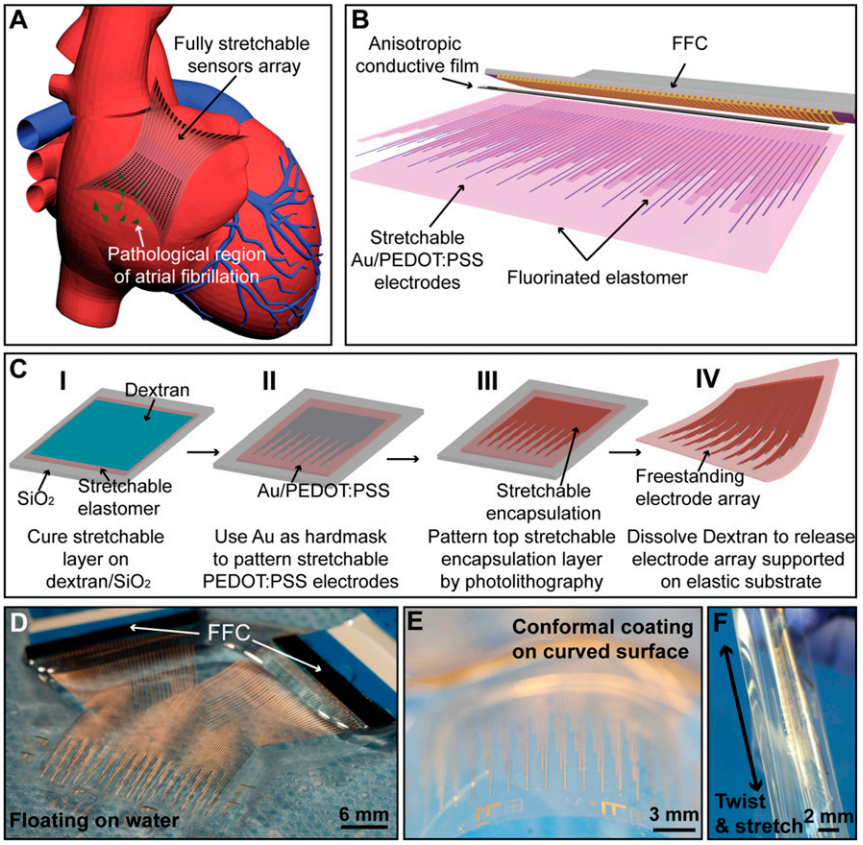

Fig. 1. Fabrication and assembly of the elastrode array for AF mapping. (*A*) Schematic showing the application of a fully stretchable elastrode array to the epicardial surface to identify the pathological regions in AF. (*B*) Schematic showing structure and connections of the elastrode array. (*C*) Schematics showing the stepwise fabrication processes of freestanding elastrode array. (*D–F*) Optical photographic images illustrating the ultralight weight (*D*), high flexibility (*E*), and stretchability (*F*) of the freestanding elastrode array.

then deposited and patterned (Fig. 1 *C*, *II*) by using a thermally evaporated gold (Au) layer as a hard mask. Next, the patterned electrodes are coated with another layer of stretchable PFPE-DMA, which is patterned by pressure-contact photolithography to define the top passivation layer for interconnections as well as to define electrode tip regions (Fig. 1 *C*, *III*). Finally, by immersing in deionized (DI) water to dissolve the dextran layer, the elastrode array is fully released from the rigid substrate (Fig. 1 *C*, *IV*). The fabricated elastrode array is then connected to a flexible cable through an anisotropic conductive film (ACF) bonded by the flip-chip bonder, as previously reported (27). To minimize the contact resistance (58 ± 12 Ω) from ACF to the PEDOT:PSS layer and to enhance the conductivity of interconnections in the non-tissue contact region, the top Au layer in the interconnections is not removed. The bonding region between the flexible cables to the elastrode array is further strengthened by a layer of PDMS curing on the top.

Fig. 1*D* shows a freestanding and fully assembled 64-channel elastrode array floating in DI water, illustrating the ultrathin and highly flexible nature of the elastrode array (5). The elastrode array has a low modulus and sub-100-μm thickness allowing it to readily conform to curved tissue surfaces (Fig. 1*E*), and it is robust enough to be stretched and twisted in different directions (Fig. 1*F*). The materials developed here for the elastrode array can be readily photopatterned with <10-μm resolution under a conventional aligner, which allows a high-density sensor array to be packaged with 64 fully connected sensors within an area of 0.25 cm^2 (*SI Appendix*, Fig. S2*A*). In this device, each sensor can be defined into a 20 × 50 μm^2 region with interconnections at 20-μm width (*SI Appendix*, Fig. S2 *B* and *C*). However, due to reduced area, the signal-to-noise ratio (SNR) is reduced, while there is no clear advantage for going much below cellular size. Therefore, the sensors used for the cardiac mapping measure 80 × 100 μm^2 in the following experiments.

Soft and Stable Epicardial Interface. A critical feature of the elastrode array is its ability to maintain mechanical and electrical properties under repeated stretching cycles, which mimic the expansion and contraction cycles of a beating heart. Fig. 2*A* shows the individual elastrode and array being stretched from 0 to 50% strain (ε) in directions that are in parallel and perpendicular to the interconnect direction. Fig. 2*B* shows the individual electrode being stretchable from 0 to 20%. Notably, the Au layer incracked into microsized "islands," while the PEDOT:PSS layers remain intact during the strain–release cycle. As the conductivity of Au is substantially higher than that of PEDOT:PSS, the microcracked Au still reduce the overall resistance of the interconnects. All of the other layers remain intact with no observed cracks or microscopic delamination based on microscopic examination. Electrochemical impedance spectrum of the sensors and interconnections (5 cm total length), when stretched from 0 to 20% strain, shows less than 10% change for the impedance (Fig. 2 *B*–*D*). The cyclic stability test further demonstrated minimal change (<5%) in mechanical resistance after 10^4 cycles of stretching to 20% strain and release (*SI Appendix*, Fig. S3). To evaluate the stability of the stretchable PFPE-DMA passivation layer in aqueous solution, we measured the electrochemical impedance of the passivation region of the device in DI water under uniaxial strain. Notably, with an 800-nm passivation layer, the impedance measured through the passivation layer was still higher than 1 GΩ under 0 to 20% strain (*SI Appendix*, Fig. S3), ∼3 orders of magnitude higher than the impedance measured through the sensing electrodes. Together, our microfabricated elastrode array demonstrates stable mechanical and electrochemical properties in aqueous solution under strains similar to those conditions expected during deformations from cardiac contractions.

To examine the potential mechanical impact to the heart tissue, we directly applied the elastrode array onto ex vivo porcine hearts. The low modulus and thin-film design allowed the device to conform well to the epicardial surface (Fig. 2*E*). The surface forces between the tissue surface and device were strong enough to adhere the device to the heart, especially in the flat ventricular region (Fig. 2*F*). Considering the complex three-dimensional (3D) anatomic geometry of the atrial free wall, we further prepared a bioelectronic bioadhesive (BOBA) gel to provide sufficient bonding force and minimize sliding at the electrode–tissue interface. The BOBA gel is a noncovalent-bonding polydopamine-based hydrogel, in which dopamine was polymerized in a polyacrylamide hydrogel network using previously reported methods (28) allowing for a nondamaging detachment from the heart. Mechanical testing showed that the BOBA hydrogel provides a fivefold higher surface-adhesion energy when compared with a regular polyacrylamide hydrogel and is strong enough to keep the device onto the surface of the heart tissue in vivo (*SI Appendix*, Fig. S4). In addition, since BOBA gel has a low modulus of kPa, its application did not affect the normal heart beating (*SI Appendix*, Fig. S4 *B*, *Inset*).

In Vivo Recording of Fast but Regular Rhythm in Dynamic Cardiac Tissues. During AF, atrial electrical activity is fast, chaotic, and uncoordinated, leading to an irregular ventricular response. The ability of the elastrode array to operate on fast-beating heart tissue was tested on rabbits with heart rates in the range of 120 to 150 beats per minute compared with the 60 to 100 beats per minute in swine (Fig. 3*A*). An *Oryctolagus cuniculus* rabbit underwent median sternotomy to expose the anterior surface of the heart, and a 64-channel elastrode array (1.4 cm^2) was placed on the ventricular epicardial surface. We observed that van der Waals forces were sufficient to provide stable adhesion at the tissue–electrode interface due to the low Young's modulus of the elastrode array (Fig. 3*B* and *SI Appendix*, Movie S1). The stretchability of the elastrode array provided a robust and intimate coupling with the fast-beating rabbit heart, providing stable high-resolution in vivo recording over the course of >10^4 stretching (10 to 20%) cycles without a decrease in signal quality (Fig. 3*C*). Importantly, we compared elastrode and a flexible, but nonstretchable, electrode with a similar softness (11 nN·m for flexible-electrodes array vs. 5.3 nN·m for elastrode array) for the in vivo cardiac recording. The results demonstrated that the elastrode array maintained its intact structure and unchanged sensor positioning, whereas the nonstretchable electrodes array had significant damage during vigorous heart movement (*SI Appendix*, Fig. S5).

Fig. 3*D* shows a representative electrogram recording from the anterior ventricular surface of the heart recorded by an elastrode array and its correlation to surface electrocardiogram (ECG) signals measured by surface contact leads. *SI Appendix*, Fig. S6 shows signals from all 64 electrodes from both ventricular and atrial surface of the heart. Furthermore, when the BOBA gel was applied to enhance the adhesion between the elastrode array and epicardium, we observed substantially improved recording efficiency (Fig. 3*E*). Specifically, the signal amplitude increased from 166.5 ± 23.1 to 520.4 ± 34.5 μV ($P < 0.0001$), the variation of the signal amplitudes (peak-to-peak amplitude) over each period of recording (2 min) was reduced from 91.4 ± 16.5 to 32.7 ± 5.6 μV ($P < 0.05$), and the SNR (amplitude of signals vs. averaged noise level) enhanced from 19.6 ± 1.8 to 102.7 ± 9.4 ($P < 0.05$) (Fig. 3 *F*–*H*). Spatiotemporal epicardial-potential data demonstrate the capture of cardiac activation propagating from the top of the array to the bottom (Fig. 3*I*), hence demonstrating our device's ability to effectively record fast cardiac signals on dynamically beating hearts in vivo.

Simultaneous Epicardial and Endocardial Electrophysiological Recording in a Porcine Model. In vivo recording of porcine hearts was undertaken to provide a more clinically relevant model. The larger displacement of the heart and stronger associated shear force had potential to damage the stretchable device, which presented

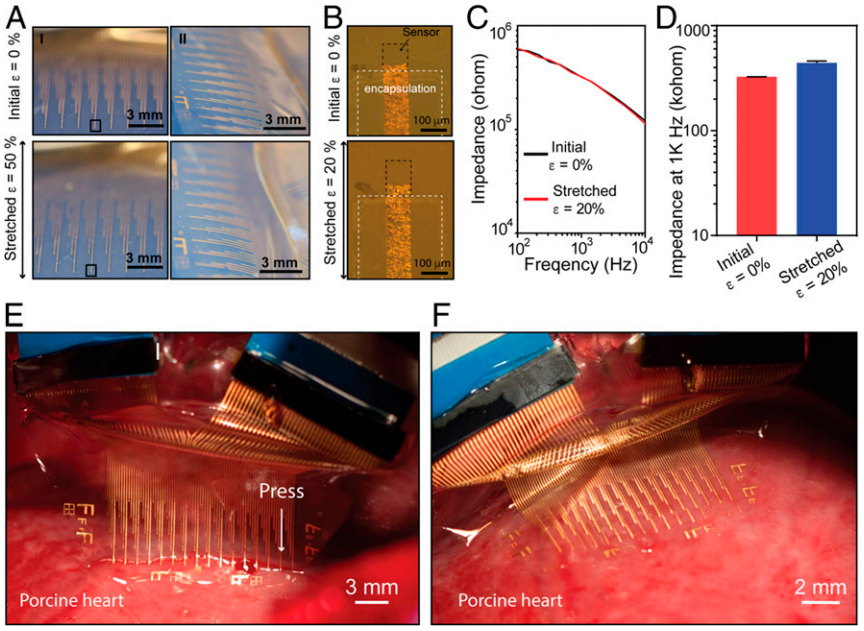

Fig. 2. Elastrode array for cardiac interface. (*A*) Optical photographic images showing the elastrode array stretched from 0 to 50% strain (ε) in directions both parallel (*I*) and perpendicular (*II*) to the interconnects. (*B*) Optical microscopic images showing an individual sensor stretched from 0 to 20% strain in the direction parallel to the interconnections. Experiments shown in Figs. 3–6 and *SI Appendix*, Figs. S3, S4, and S6–S8 used electrodes with the same dimensions as shown here. (*C*) Impedance spectrum of a representative elastrode stretched from 0 to 20% strain in the direction parallel to the interconnections. (*D*) Statistic result of 20 sensors stretched from 0 to 20% strain in the direction parallel to the interconnections. Data represent means ± SEM. (*E*) Optical photographic image showing the array in partial contact with the porcine RV. (*F*) Optical photographic image showing the array in a full contact with the RV.

additional technical challenges. Hence, we removed the bottom PDMS layer and used PFPE-DMA as both the substrate and the tip passivation layer. We found that due to the strong adhesion forces between the two perfluorinated layers, the elastrode array had stronger stability and avoided any delamination within its multilayered structure. Then, we applied the improved elastrode arrays to the porcine model and performed correlated epicardial and endocardial mapping of the right atria (RA) through application of the elastrode array on the epicardial surface and placement of a commercially available basket-shaped 64-channel diagnostic mapping catheter (FIRMap; Abbott, St. Jude) on the endocardial surface of the RA (basket-electrodes array) (Fig. 4 *A*–*C*). The intrinsic stretchability of the elastrode array effectively prevented sliding and delamination from the epicardial surface during expansion/contraction of the right atrium (RA) in vivo (Fig. 4*D*). Single voltage recordings (Fig. 4*E* and *SI Appendix*, Fig. S7) showed enhanced and clear atrial signals from the elastrode array on the RA compared with the right ventricle (RV). Notably, the sensing area of an elastrode is approximately 1,000 times smaller than the corresponding coverage of the basket electrode. While this smaller area results in a higher interface impedance and slightly smaller peak-to-peak signal amplitudes (228.1 ± 28.1 μV vs. 308.0 ± 31.6 μV, for the elastrodes and basket electrodes, respectively), the ratio between atrial and ventricular signals was significantly higher ($P < 0.0001$) for the elastrodes (0.87 ± 0.02) as compared with the basket electrodes (0.44 ± 0.04) (Fig. 4*F*).

Fig. 4*G* shows representative raw traces of epicardial elastrode recordings and endocardial basket-electrode recordings under pacing. The activation times were determined by using the maximum negative slope (dV/dt) of each electrogram to generate isochronal maps. The isochronal map (Fig. 4*H*) indicated that the velocity of the action potential propagation recording on the surface of heart is 1.16 m/s, which is comparable to previously reported values on large-scale recording (5, 12). In addition, we placed a pacing electrode on the atrial appendage to send an electrical signal in the opposite direction of normal atrial-signal propagation and generated the isochronal map, which showed the signal propagated in the opposite direction (*SI Appendix*, Fig. S8). Together, these results show the reliable signal recording and activation mapping by using the elastrode electrode array.

Simultaneous Epicardial and Endocardial Mapping during Chronic AF. Next, we performed mapping in a porcine model of chronically stable AF using methods previously described (27). *Sus scrofa* pigs underwent pacemaker implantation followed by chronic atrial pacing at 350 beats per minute with an amplitude of 10 mA for 6 wk to induce chronically stable AF (Fig. 5*A*). Persistent AF was confirmed with ECG after 6 wk of pacing, and the pigs were maintained for an additional 4 wk before conducting terminal cardiac-arrhythmia mapping.

Surgery and placement of the elastrode array and basket electrodes was performed following the same procedures as described for the acute porcine surgeries. Fig. 5*B* shows the representative voltage traces from ECG leads, elastrode arrays, and basket-electrode arrays. Activation times were calculated for two 100-ms intervals where atrial signals were identified (Fig. 5 *C* and *I*, *II*). To compare activation time-delay patterns in the overlapping region covered by both the elastrode array and the basket electrodes (dashed boxes in Fig. 5*D*), isochronal maps of activation times were plotted using the same temporal reference and scale (Fig. 5*E*). Notably, the activation maps generated from the basket electrodes showed heterogeneous activation patterns with up to 100-ms delay. Meanwhile, all channels from the elastrode array showed a range of activation-time delays that corresponded to those calculated from the basket electrodes (dashed boxes highlighted in Fig. 5 *D* and *E*). More importantly, after adjusting the temporal scale of activation maps from the elastrode array, we can observe finer patterns of localized electrical heterogeneity within the 10- to 30-ms time scale, revealing more heterogenous activities that are happening at the substrate between two basket electrodes, which was not captured before (Fig. 5*F*).

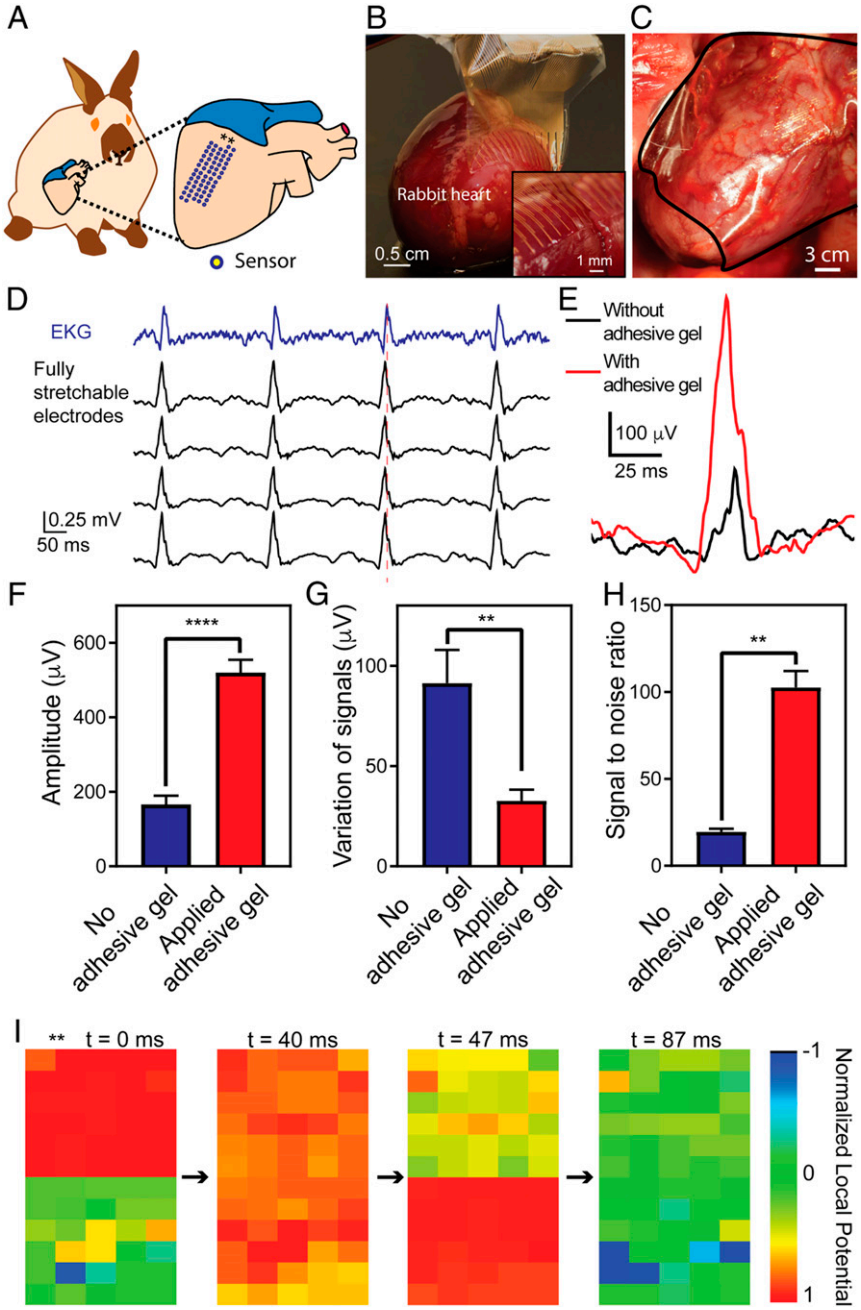

Fig. 3. In vivo epicardial recording on rabbit. (*A*) Schematic showing the relative position of the elastrode array on the surface of a rabbit heart. Stars label the orientation of the elastrode array. (*B*) Optical photographic image demonstrating the freestanding elastrode array conforming to the surface of superior RV of an ex vivo rabbit heart via surface tension. *Inset* shows the sensor region conforming on the surface of the heart. (*C*) Optical photographic image showing the elastrode array conforming to the surface of superior RV of heart from a rabbit through a median sternotomy. The black line highlights the region of the device. (*D*) Representative voltage traces of the ECG from surface contact leads (black) and electrograms from the elastrode array on the surface of rabbit anterior RV (blue). All 64-channel signals are shown in *SI Appendix*, Fig. S6. The red dashed line highlights the time delay between ECG and electrogram from elastrode array. (*E*) Representative single voltage traces showing individual spikes from electrograms before and after applying BOBA gel to enhance the adhesion between the elastrode array and the heart. (*F–H*) Statistical analysis of amplitude (*F*), stability (variation of signal amplitude over 1 min) (*G*), and SNR of signals (*H*) before and after applying BOBA gel ($n = 32$). $^{**}P < 0.01$; $^{****}P < 0.0001$. All data are means ± SEM. Statistical analysis was performed by paired *t* test. (*I*) Representative normalized voltage data for 60 channels (channels 1 to 30 and 33 to 62 in *SI Appendix*, Fig. S6) on the elastrode array as their relative position to the heart shown in *A* at 4 points in time showing a normal cardiac wavefront propagation. Normalized voltage is plotted with the color scale on the right. Stars show the orientation of the elastrode array corresponding to that in *A*.

Correlation and Mapping of Epicardial and Endocardial Heterogeneity during Chronic AF. Further proving the correlation of signals between elastrode array and basket electrodes, we calculated the correlation of the power spectrum between two sets of signals. Notably, we observed correlation between the elastrode-array recording region and basket-electrode channel 1 from both the imaging and the power spectrum (Fig. 6*A*). The frequency mapping showed the same level of base frequency from signals recorded by elastrodes as that recorded by channel 1 on the basket electrodes (Fig. 6*B*). In order to compare the quality of electrogram recordings from

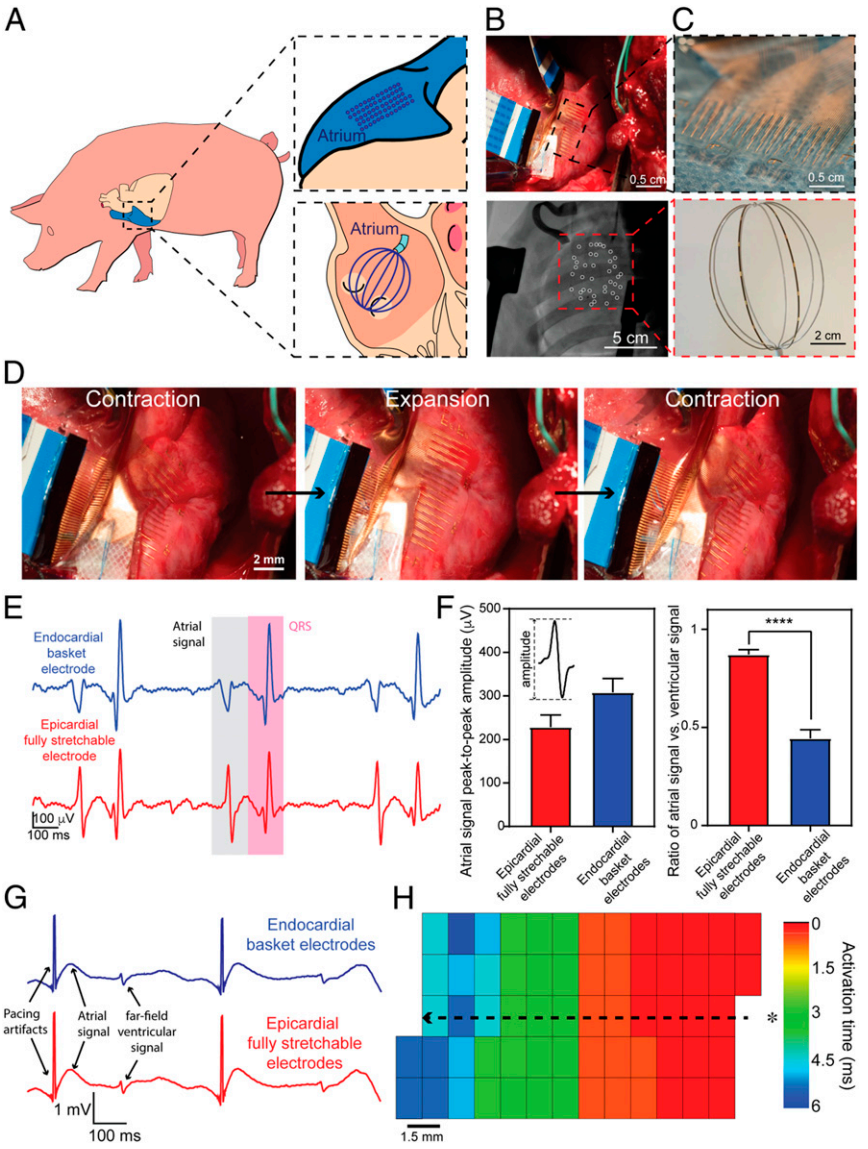

Fig. 4. Simultaneous in vivo epicardial and endocardial recording on porcine atrium. (*A*) Schematics showing relative positions of an elastrode array placed on the surface of RA (*Right*, *Upper*) and a basket electrode (*Right*, *Lower*) placed inside the RA, respectively. (*B*) Optical photographic image of a representative elastrode array on the surface of the superior RA (*Upper*) and a fluoroscopic image of a representative basket electrode placed inside the RA (*Lower*). White circles highlight all of the visible basket electrodes. (*C*) Photograph of the epicardial elastrode array, with the *Inset* showing the micrometer-scale electrical sensor (*Upper*), and optical photographic image of the endocardial basket electrode, with *Inset* showing the millimeter-scale electrical sensor (*Lower*). (*D*) A series of images showing one cycle of the in vivo contraction–expansion for the RA during the electrogram mapping. (*E*) Representative single voltage tracing from an endocardial basket electrode (blue) and epicardial elastrode (red) from the RA during sinus rhythm. (*F*) Statistical analysis of the amplitude (*Left*) and the ratio of the atrial signal to the ventricular signal (*Right*) from both epicardial and endocardial electrodes. Statistical analysis was performed with unpaired *t* test ($n = 32$, $P < 0.0001$). (*G*) Representative single voltage trace from the atrial surface paced from a stretchable electrode gives comparable waveform as a standard clinical electrode. (*H*) Color map shows relative activation-time mapping from the epicardial elastrode array with external pacing, showing that the signal travels away from the external source. This indicates that the stretchable electrode array is capable of capturing atrial signals, and activation maps generated are consistent with what we expect under normal physiological and external electric-signal stimulation conditions. The asterisk (*) indicates the relative location of the external pacing electrode. The dotted line with the arrow indicates the directionality of electric-signal progression from the pacing electrode.

each electrode array to address the heterogeneity of cardiac activity in AF, the correlation coefficients of the signal morphology and power spectrum of the ECG with every other electrogram within the same device were calculated. A high correlation coefficient indicates that there is a large percentage of signals with similar frequency and morphology, suggesting that those signals are more homogeneous and likely arising from a similar source. A lower correlation coefficient indicates that the signals are more heterogeneous. The results demonstrated (Fig. 6 *C*–*F*) a much higher correlation coefficient between the elastrodes as compared with that from basket electrodes. Results showed a statistically significantly higher correlation (0.72 ± 0.01) coefficient between all elastrode (*SI Appendix*, Fig. S9) channels to basket electrodes channel 1 than that to other channels.

Our results (Fig. 6 *C* and *E*) show a clear correlation between signals from most channels on the high-density elastrode array. In contrast, the signals from the basket electrodes had little or no

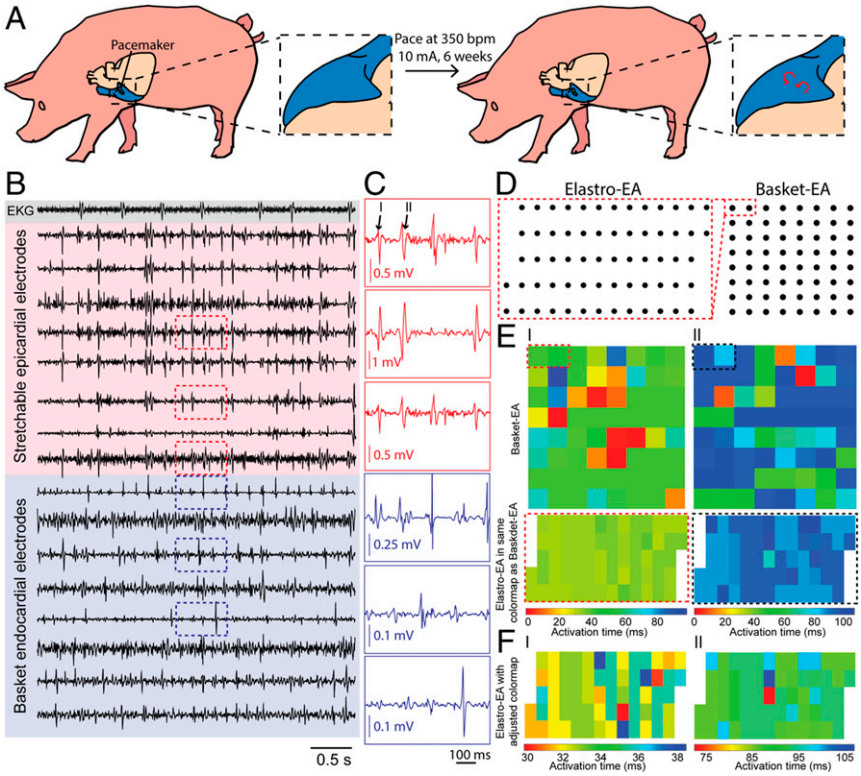

Fig. 5. Simultaneous epicardial and endocardial mapping of chronic AF. (*A*) Schematic showing pacing-induced persistent AF in a porcine model. (*B*) Representative voltage traces from ECG electrode (gray), epicardial elastrode array (red), and endocardial basket electrode (blue). (*C*) Representative voltage traces of regions outlined by red and blue dashed boxes in *B* highlighting the individual peaks (black numbers labeled) that we used to create activation mappings in *E*. (*D*) Relative positions of the epicardial elastrode array to endocardial basket electrodes. (*E*) Isochronal maps of activation time from endocardial basket electrodes (*Top*) and the epicardial elastrode array (*Bottom*) from the same temporal reference and scale. Dashed boxes highlight the relative position of the elastrode array to the basket electrode during recording. Each pair of activation maps from the basket electrode and elastrode array is calculated respective to the same temporal reference. Numbers correlate each mapping to the peak highlighted in *C*. (*F*) Activation maps of the epicardial elastrode array with adjusted time scale highlighting the local variation of signals. Values on the activation time scale correspond to values in *E*.

correlation owing to their wide spacing (Fig. 6 *D* and *F*). The above results suggest that while the basket electrodes gives us the initial and final snapshot of signals between two widely spaced points on the heart tissue, the high-density elastrode array is capable of capturing finer details of the signal variation, which can then help to identify where the exact points of heterogeneity occur and in what way the signals are changed. Fluoroscopic imaging was used to illustrate the relative position between the elastrode array, basket electrodes, and atria during the experiments (*SI Appendix*, Fig. S10*A*). Finally, the atrium was reconstructed from noninvasive MRI imaging, and electroanatomical correlation was achieved by projecting isochrones activation maps on the surface of the RA (*SI Appendix*, Fig. S10*B*).

Discussion

In conclusion, the results presented here demonstrate a fully stretchable and encapsulated elastrode array capable of performing high spatiotemporal cardiac mapping in vivo. The electronic materials used in our elastrode array display a tissue-mimetic modulus and intrinsic stretchability, enabling the elastrode array to adhere to the epicardium of the heart with the assistance of a noncovalent hydrogel. The elastrode array provides a stable localized signal recording from in vivo heart tissue and is capable of mapping electrogram on complex geometries, such as those seen in the atrial regions, which are hard to access using conventional tools. The elastrode array exhibits the capacity to reliably record localized, high-density electrograms during rapid sinus rhythm in the rabbit, where the ventricle goes through 150 cycles of expansion and contraction per minute. More importantly, we demonstrate the capability to reliably record signals strong enough to be used for activation time calculation and mapping to identify clinically relevant arrhythmogenic regions in the pathologic state of acute AF, where the signals on the atrium not only are of much smaller amplitude compared with those of the surrounding ventricular region but also have a much more irregular pattern at the cellular level.

We also compared our recording with current commercially available diagnostic mapping electrode arrays. Here, we show that we are able to achieve higher-density mapping with an order of magnitude increase in electrode density while maintaining comparable or higher signal quality. Through comapping with the endocardial basket electrodes, our device is able to further identify heterogeneous activation between epicardial and endocardial surfaces as well as between different electrodes within the electroanatomic recordings produced by the basket electrodes through the high-density electrodes, providing higher spatial resolution on the epicardial recording. Taken together, our approach underscores the potential use of complementary mapping strategies utilizing a high-density elastrode array and conventional endocardial-basket electrodes to further our clinical understanding and treatment of AF.

Both the electronic materials and fabrication processes developed in this study are readily scalable and can be applied to electrical connection and encapsulation of the high-density multiplexing circuits. To this end, we highlight the capability of creating a fully stretchable electrode array comprised of

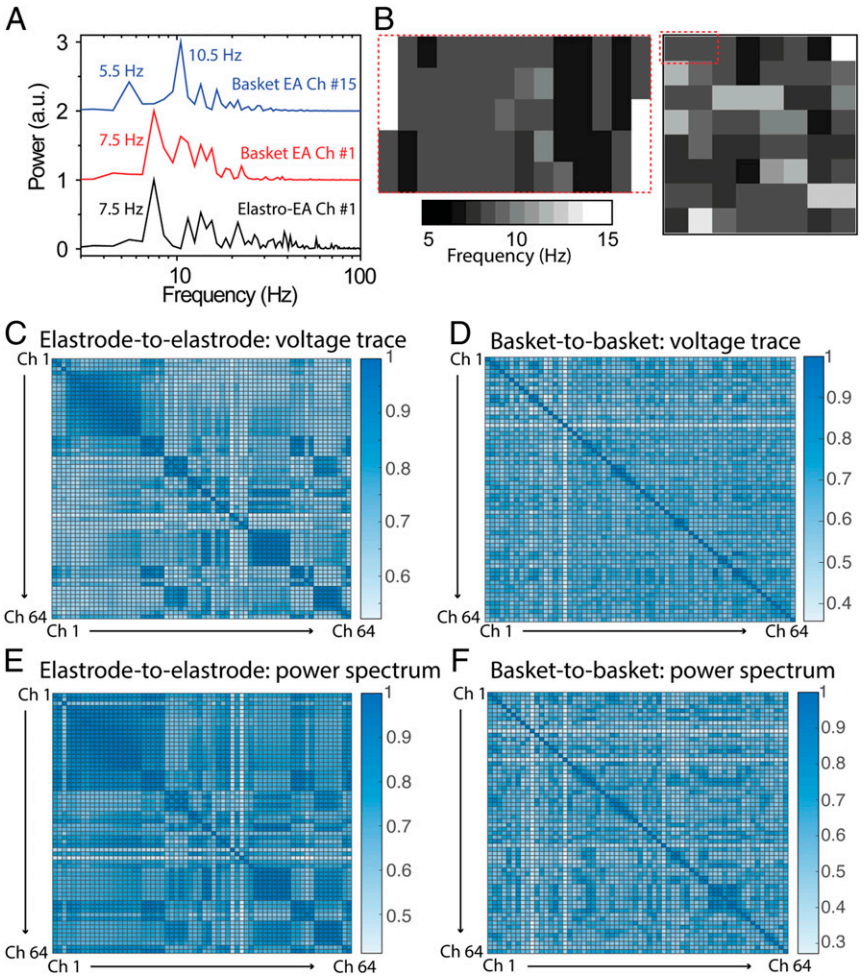

Fig. 6. Correlation of epicardial and endocardial mapping of chronic AF. (*A*) Power spectrums of representative epicardial and endocardial signals. (*B*) Power spectrum mapping of epicardial and endocardial signals. (*C–D*) Heat plot of the cross-correlation matrix of the raw voltage trace of epicardial signals between each elastrode (*C*) and each basket electrode (*D*). (*E* and *F*) Heat plot of the cross-correlation matrix of the power spectrum of epicardial signals between each elastrode (*E*) and each basket electrode (*F*).

thousands of sensing units to encompass the entire atrial epicardium to capture both global and local arrhythmic activities. This high-throughput and high-density device should facilitate both mapping and elucidating the mechanisms of arrhythmias in both animal models and patients. Finally, recent studies (29–32) have suggested that foreign-body responses were substantially minimized when using tissue-like electronics for long-term implantation. Our elastrode array would thus represent an ideal candidate for chronic implantation on the epicardium given its tissue-compatible mechanical properties. Such long-term measurement of signals at the cellular level would allow us to better understand the mechanism and eventually help guide new surgical treatments of AF.

Materials and Methods

Materials Synthesis.

Preparation of PEDOT:PSS/IL mixture. PEDOT:PSS (PH1000) and the ionic liquid (IL) bis(trifluoromethane)sulfonimide lithium salt were purchased from Clevios and Santa Cruz Biotechnology, respectively. About 50 wt% of IL vs. PEDOT:PSS was added to PEDOT:PSS aqueous solution (0.172 g in 15 mL of PH1000 solution) and stirred vigorously for 20 min. The PEDOT:PSS/IL aqueous mixture was then filtered by a 0.45-μm syringe filter.

Synthesis of PFPE-DMA. The synthesis of dimethacrylate-functionalized perfluoropolyether monomer (PFPE-DMA) is the same as described in a previous report (33). Briefly, the PFPE diols (4 kg/mol) were obtained from Solvay Specialty Polymer. It was first dissolved in 1,1,1,3,3-pentafluorobutane and reacted at room temperature with isophorone diisocyanate at a 2:1 molar ratio for 48 h to yield the chain-extended PFPE diols. Then, the product reacted with 2-isocyanatoethyl methacrylate (IEM) at a 1:1 molar ratio (4 kg/mol PFPE diols:IEM) at room temperature for 48 h. In both reactions, 0.1 wt % tetrabutyltin diacetate was used as the catalyst. The final product was filtered through a 0.2-μm syringe filter to yield clear and colorless oil. The solvent was removed by rotary evaporation.

Synthesis of BOBA hydrogel. Acrylamide (1.18 g) (no. A9099; Sigma-Aldrich), 0.7 mg of bisacrylamide (no. A3699; Sigma-Aldrich), and 24 mg of ammonium persulfate (no. A3678; Sigma-Aldrich) were dissolved in 8.6 mL of DI water. Then, 20 μL of tetramethylethylenediamine (no. A3678; Sigma-Aldrich) was added to allow the gel to be formed in a glass Petri dish. After the gel formed, 250 mg of dopamine (no. H8502; Sigma-Aldrich) in 50 mL of 1 M tris(hydroxymethyl)aminomethane hydrochloride buffer (no. 15568025; ThermoFisher Scientific) was added to the gel. After a 24-h reaction, the gel was rinsed with water to remove any extra dopamine. The gel can be readily peeled off from Petri dish for the further usage. The gel without dopamine was used as a control sample for the following research.

Device Fabrication and Assemble.

Elastic electrodes (elastrode) array fabrication. A dextran (no. 09184; Sigma-Aldrich) aqueous solution (5 wt%) was spin-coated on a Si wafer as the sacrificial layer (2); 8 kg/mol PFPE-DMA dissolved in 1,3-bis(trifluoromethyl) benzene (99%; no. 251186; Sigma-Aldrich) solution was spin-coated on a PDMS film on top of the dextran layer at 1,500 rpm for 1 min in a N_2 glovebox (mBRAUN Glove Box System). The PFPE-DMA layer was then ultraviolet (UV)-cured (UV nail lamp, 340- to 380-nm wavelength, 36 W) for 5 min,

followed by baking at 180 °C for 1 h and subsequently treated with the oxygen plasma (Technics Micro-RIE Series 800) at 150 W for 1 min (3). The PEDOT:PSS/ionic liquid aqueous mixture was spin-coated (2,000 rpm, 1 min) on the oxygen plasma-treated PFPE-DMA layer and baked at 120 °C for 30 min. Then, the PEDOT:PSS/ionic liquid film was treated with DI water to remove the extra ionic liquid (4); 40 nm of Au was subsequently deposited by thermal evaporator evaporation (KJ Lesker evaporator) (5). S1805 photoresist was then spin-coated on Au at 4,000 rpm for 45 s and exposed with mask aligner (Quintel Q4000) for 3 s at a power of 10 mW/cm^2 after 1-min, 115 °C preexpose baking. The exposed photoresist was developed in the CD-26 developer (Micropost; Shipley) for 1 min (6). Micropatterns of S1805 were transferred to Au by etching using argon ion milling (bias voltage, 100 V; Intlvac Nanoquest Ion Mill) for 1 min. Inductively coupled plasma etch system (600 W, 80 standard cubic centimeters per minute [sccm]; PlasmaTherm Oxide Etcher) or oxygen plasma (300 W, 8 sccm; March PX-250 Plasma Asher) was used to etch PEDOT:PSS film and remove the photoresist (7). The Au layer on PEDOT was removed by the argon ion milling etching for 1 min or left on the top of PEDOT:PSS to enhance the conductivity (8). The PFPE-DMA solution with 2 wt% photoinitiator bis(2,4,6-trimethylbenzoyl)-phenylphosphine oxide (no. 511447; Sigma-Aldrich) in bis(trifluoromethyl)benzene (1 g/mL) was spin-coated at 1,000 rpm for 1 min and then prebaked at 100 °C for 1 min. A UV exposure (350 to ∼450 nm; Quintel Q4000 Hg Lamp) at 10 mW/cm^2 for 10 s was used to pattern PFPE-DMA as the top passivation layer and define the sensor region. For imaging samples used in the biocompatibility test, rodamine-6G (1 μg/mL; no. 252433; Sigma-Aldrich) was added in the PFPE-DMA solution as the top passivation. The UV-exposed PFPE-DMA was developed in 1,3-bis(trifluoromethyl)benzene for 1 min.

Integrate freestanding elastrode array for recording. The input/output (I/O) connection pads at the end of the elastrode array were bonded to a flexible cable through ACF (1). A piece of ACF (CP-13341-18AA; Dexerials America Corporation, San Jose, CA), 1.5 mm wide and 15 mm long, was over the I/O pads and partially bonded for 10 s at 75 °C and 1 MPa using a commercial bonder (Fineplacer Lambda Manual Sub-Mm FlipChip Bonder; Finetech, Inc., Manchester, NH) (2). A flexible cable (FFC/FPC Jumper Cables PREMO-FLEX; Molex, Lisle, IL) was placed on the ACF, aligned with I/O pads, and bonded for 1 to 2 min at 165 to 200 °C and 4 MPa (3). PDMS was coated on the bonding region and cured at 70 °C overnight to protect the bonding regions (4). The bonded device was immersed in DI water for 1 h to be released from the wafer and dried on a tissue paper.

To validate an effective contact and measure the contact resistance of the bonding on the stretchable Au/PEDOT:PSS electrodes, electrodes of the same size were patterned following the same procedure described above on the top of the PFPE-DMA film on the Si wafer without the top passivation layers. After bonding, voltage meter was used to measure the contact resistance across the ACF bonding.

Device Characterization.

Morphological characterization. Optical imaging was carried out on a Leica upright optical microscope. Specifically, a free-standing elastrode array was stretched by a home-built stretcher and imaged under an upright optical microscope.

Electrical and electrochemical characterization under uniaxial stretching. The electrochemical impedances were measured with a potentiostat (Biologic VSP-300 workstation) in the phosphate-buffered saline (PBS) (0.1 M, pH 7.4) solution. A platinum electrode was used as the counter electrode. The potentiostatic electrochemical impedance spectroscopy was measured with a sine wave (frequency from 1 Hz to 1 MHz) and a signal amplitude of 10 mV; 20% strain and cycles of strains was applied to the device during the measurement based on a home-built stretcher published previously (34).

Mechanical characterizations. Mechanical strain–stress of the device was performed using an Instron 5565 measurement set-up. To test the gel adhesion on the epicardium, a porcine heart tissue (2 cm × 5 cm × 0.5 cm) was glued to a glass substrate. BOBA hydrogel and control sample with the same dimension were glued to another glass substrate. These two substrates were brought into contact, and the force was measured using an Instron 5565 measurement set-up with the 100-N loading cell. The adhesion strength was calculated with the force and the contact area.

Thickness of PFPE-DMA characterization. The PFPE-DMA was photopatterned on a rigid substrate such as a Si wafer. After development and postbaking, a profilometer (Bruker Dektak XT; Bruker Inc.) was used to map the thickness of PFPE-DMA across the Si wafer.

Animal Experiments.

Animal preparation. All studies were approved by the Stanford University Administrative Panel on Laboratory Animal Care and were conducted in compliance with guidelines for animal experimentation. Domestic *O. cuniculus* rabbits (Charles River Laboratory) and *S. scrofa* pigs (40 to 50 kg; Pork Power Farms) were used for this study.

The goal of employing a rabbit model into this study is to 1) test the performance of an elastrode array on a rapidly beating heart without the large spatial displacement and 2) cover a relatively larger area on the animal heart with a high-density epicardial sensor array to record signals from different regions of heart (e.g., atrium vs. ventricle). The goal of employing the porcine model in this study is to 1) conduct simultaneous epicardial and endocardial recording, 2) compare the performance of a micrometer-scale elastrode array with the commercially available, millimeter-scale basket electrodes at the same time on the same biological replicate, and 3) allow the implementation of the pacing-induced sustained AF disease model.

Cardiac mapping during normal sinus rhythm in a rabbit model. Domestic *O. cuniculus* rabbits were premedicated with Telazol plus ketamine plus xylazine (TKX) (1 mL per 50 to 75 kg; Telazol powder plus 250 mg of ketamine [100 mg/mL] plus 250 mg of xylazine [100 mg/mL]), preoxygenated, induced with propofol 5 to 12 mg/kg, intubated, and maintained with a ventilator with 100% O_2. The rabbit was monitored throughout the entire procedure with ECG, oxygen saturation, and arterial pressure throughout the procedures. After anesthesia, the rabbit heart was exposed via median sternotomy. ECG signals were recorded via four body surface leads on the right arm, left arm, right leg, and left leg throughout the experiment as a reference. Unipolar voltage data from the epicardial surfaces were recorded at the same time with the ActiveTwo System (BioSemi, Amsterdam, The Netherlands). All signals were sampled at 1,024 Hz and digitized at 24 bits. The elastrode array placed on the top of the rabbit posterior RV and RA. The BOBA gel was placed on the top of the device to wrap around the rabbit's heart, gluing the device to the heart. At the conclusion of the study, the animal was killed humanely with a concentrated potassium chloride solution.

In vivo epiendocardial mapping during pacing and acutely paced AF in a porcine model. *S. scrofa* pigs were premedicated with Telazol plus ketamine plus xylazine (TKX) (1 mL per 50 to 75 kg; Telazol powder plus 250 mg of ketamine [100 mg/mL] plus 250 mg of xylazine [100 mg/mL]), preoxygenated, induced with propofol 5 to 12 mg/kg, intubated, and maintained with a ventilator with 100% O_2. The pig was monitored throughout the entire procedure with ECG, oxygen saturation, and arterial pressure throughout the procedures. In a typical experiment, one 60-kg female pig underwent median sternotomy. A basket with 64 channels with an interelectrode distance of 0.5 cm was inserted through the superior vena cava and opened inside the RA for the endocardial recording throughout the entire experiment. The position of basket catheter was verified using computerized tomography under fluoroscopy.

The elastrode array and BOBA gel were placed in the same manner as described in *Cardiac Mapping during Normal Sinus Rhythm in a Rabbit Model*. Two bipolar electrodes were sutured onto the superior RA free wall. Pacing threshold was measured at the beginning, and subsequent pacing with Bloom Stimulator DTU-215B (Fischer Medical, Broomfield, CO) was conducted with at least twice that threshold. For inducing acute AF, 30-s cycles of eight stimuli with a basic cycle length of 300 ms (S1) followed by a single extra stimulus (S2) were used, and S1 cycle length decreased by 50 ms every cycle until reaching 100 ms. When the animal still did not fibrillate, burst pacing with a cycle length of 100 ms was used. Epi- and endocardial signals were recorded simultaneously from the elastrode array and basket electrodes using the same method described above. After the surgery, the animal was killed, and the heart was removed en bloc for gross and immunohistological assessment. The section where elastrode patches recorded from was fixed in methanol for the immunohistology and microscopic examination for structural changes.

In vivo cardiac arrhythmic mapping in a chronic stable AF porcine model. *S. scrofa* pigs received pacemaker implantation for chronic pacing in order to achieve induced stable AF and subsequently underwent cardiac arrhythmic mapping. Cardiac gated MRI reviewed a normal heart with minimal scarring. Under general anesthesia, two standard pacing leads (St. Jude Medical 2210, Minneapolis, MN) were placed into the RA appendage under fluoroscopic guidance and secured. The pacemaker (St. Jude Medical) was connected to the pacing leads and buried in a subcutaneous pocket. Daily oral aspirin (81 mg) was given for stroke prevention, and daily digoxin (0.25 mg with 0.25 mg increment every 2 wk) was administered to maintain ventricular rate during high-rate pacing until the terminal procedure. The animal was continuously paced at 350 beats per minute with amplitude of 10 mA for 6 wk. The pacer was then shut off, and the animal remained in stable AF. The animal was maintained for 4 more weeks until it underwent the terminal procedure for cardiac arrhythmic mapping.

During in vivo mapping, the animal went through general anesthesia and median sternotomy as described in *In Vivo Epiendocardial Mapping during Pacing and Acutely Paced AF in a Porcine Model* to expose the heart. Then, the pacer leads were removed and 64 basket electrodes were inserted for endocardial recording. A large low-density molded silicone plaque with 64 unipolar electrodes was first placed on the RA epicardial surface. The electrode templates were constructed from a form-fitting silicon elastomer (Specialty Silicone Fabricators, Paso Robles, CA) that fit on the entire curvilinear surface of RA and contained 0.5-mm-diameter silver electrodes (Pacific Wire & Cable, Inc., Santa Ana, CA) with an interelectrode distance of 5 mm. Placement of epi- and endocardial electrodes were confirmed with fluoroscopic system (Allura XPER Biplane; Philips, The Netherlands). Simultaneous epi- and endocardial data from RA were first recorded. Then, the elastrode array was place on the RA for recording based on the arrhythmia region identified by the silver electrodes array.

Data were recorded and processed using the same method as described above. After the surgery, the animal was killed, and the heart was removed en bloc for gross and immunohistological assessment. The section where elastrode patches recorded from was fixed in methanol for the immunohistology and microscopic examination for structural changes.

Data Analysis. Data from all channels were processed in custom-designed MATLAB software. A filter with a bandwidth of 30 to 300 Hz was applied for the electrogram data. A filter with 4 to 10 Hz was applied for the ECG. The average of all 64 electrograms from the respective mapping method was used as a referenced signal for the subtraction. Activation times were automatically detected by calculating the maximal absolute (positive and negative) slope of voltage over time *(dV/dt)* and were individually manually reviewed and edited for accuracy. Channels with poor contact were removed, and data were interpolated. The results were used to generate normalized voltage and isochronal maps showing wavefront propagation and activation-time delay in space and time across the sensor array. The power spectrum, channel correlation, and spectrum analysis were generated by home-built MATLAB code. The mappings were plotted by OriginPro 8.1.

Immunostaining and Confocal Imaging. The heart section was fixed overnight using methanol. The fixed section was washed with PBS for three times to remove the extra methanol. Then, the section was mounted on a vibrotome to be sliced into 50-μm slices. The samples were then permeabilized by 0.1% Triton-X 100 in PBS for 1 h. After washing with PBS, the samples were incubated in blocking solution (3% bovine serum albumin, 0.1% Triton-X 100 in PBS) overnight. The samples were then costained with anti–α-actinin mouse monoclonal antibody (1:200; Clone EA-53; Sigma-Aldrich Corp., St. Louis, MO) and AlexaFluor-647 goat anti-mouse (1:200; Molecular Probes, Invitrogen, Grand Island, NY) as the primary and secondary antibodies, respectively. DAPI was used to counter-stain cell nuclei. The stained slices, after being washed with PBS, were placed on the top of the device and fixed by the PDMS on the side. The device/tissue hybrids were placed on the inverted Leica LSM 789 laser-scanning microscope and fixed by the imaging station. The strain was applied to whole sample imaged by 20× water-immersion lens.

Reconstruction of the Heart Model Using MRI. Prior to chronic mapping surgery, four-chamber cardiac MRI imaging was obtained using the MRI system (Signa 3T; GE Healthcare, Chicago IL) with late gadolinium enhancement. The MRI files were converted to a 3D model using a custom-developed software package. The atria were manually segmented, and then the electrical mapping data were projected onto the epicardial surface of the RA to display variations in surface voltage.

Data Availability. All data needed to support the conclusions presented in this paper are available in the manuscript and/or *SI Appendix*.

ACKNOWLEDGMENTS. We thank X. Liu, Y. Li, and K. Zhang from the BOE Technology Group Co., Ltd., for discussions and Daikin Co. and Solvay for supplying PFPE diols. We thank Drs. S. Baker and C. Pacharinsak from the Veterinarian Service Center and Department of Comparative Medicine for their tremendous help with the animal model and surgery. This work was partly supported by a Bio-X Interdisciplinary Initiatives Seed Grant and by BOE Technology Group Co., Ltd. Part of this work was performed at the Stanford Nano Shared Facilities, supported by NSF Award ECCS-1542152. X.Z. is supported by the Stanford Cardiovascular Institute Dorothy Dee & Marjorie Helene Boring Trust Award. Y.L. is supported by the National Science Scholarship (Agency for Science, Technology and Research, Singapore).

1. S. S. Chugh *et al*., Worldwide epidemiology of atrial fibrillation: A Global Burden of Disease 2010 Study. *Circulation* **129**, 837–847 (2014).
2. M. Haïssaguerre *et al*., Spontaneous initiation of atrial fibrillation by ectopic beats originating in the pulmonary veins. *N. Engl. J. Med.* **339**, 659–666 (1998).
3. M. Haïssaguerre *et al*., Catheter ablation of long-lasting persistent atrial fibrillation: Critical structures for termination. *J. Cardiovasc. Electrophysiol.* **16**, 1125–1137 (2005).
4. T. Rostock *et al*., High-density activation mapping of fractionated electrograms in the atria of patients with paroxysmal atrial fibrillation. *Heart Rhythm* **3**, 27–34 (2006).
5. A. M. Lee *et al*., Importance of atrial surface area and refractory period in sustaining atrial fibrillation: Testing the critical mass hypothesis. *J. Thorac. Cardiovasc. Surg.* **146**, 593–598 (2013).
6. S. M. Narayan, K. Shivkumar, D. E. Krummen, J. M. Miller, W. J. Rappel, Panoramic electrophysiological mapping but not electrogram morphology identifies stable sources for human atrial fibrillation: Stable atrial fibrillation rotors and focal sources relate poorly to fractionated electrograms. *Circ. Arrhythm. Electrophysiol.* **6**, 58–67 (2013).
7. J. Jalife, O. Berenfeld, M. Mansour, Mother rotors and fibrillatory conduction: A mechanism of atrial fibrillation. *Cardiovasc. Res.* **54**, 204–216 (2002).
8. G. Lee *et al*., Epicardial wave mapping in human long-lasting persistent atrial fibrillation: Transient rotational circuits, complex wavefronts, and disorganized activity. *Eur. Heart J.* **35**, 86–97 (2014).
9. P. Podziemski *et al*., Rotors detected by phase analysis of filtered, epicardial atrial fibrillation electrograms colocalize with regions of conduction block. *Circ. Arrhythm. Electrophysiol.* **11**, e005858 (2018).
10. S. Nattel, D. Dobrev, Controversies about atrial fibrillation mechanisms: Aiming for order in chaos and whether it matters. *Circ. Res.* **120**, 1396–1398 (2017).
11. C. R. Barbhayia, S. Kumar, G. F. Michaud, Mapping atrial fibrillation: 2015 update. *J. Atr. Fibrillation* **8**, 1227 (2015).
12. J. Viventi *et al*., A conformal, bio-interfaced class of silicon electronics for mapping cardiac electrophysiology. *Sci. Transl. Med.* **2**, 24ra22 (2010).
13. H. Fang *et al*., Capacitively coupled arrays of multiplexed flexible silicon transistors for long-term cardiac electrophysiology. *Nat. Biomed. Eng.* **1**, 38 (2017).
14. X. Dai, W. Zhou, T. Gao, J. Liu, C. M. Lieber, Three-dimensional mapping and regulation of action potential propagation in nanoelectronics-innervated tissues. *Nat. Nanotechnol.* **11**, 776–782 (2016).
15. D. H. Kim *et al*., Electronic sensor and actuator webs for large-area complex geometry cardiac mapping and therapy. *Proc. Natl. Acad. Sci. U.S.A.* **109**, 19910–19915 (2012).
16. D. H. Kim *et al*., Materials for multifunctional balloon catheters with capabilities in cardiac electrophysiological mapping and ablation therapy. *Nat. Mater.* **10**, 316–323 (2011).
17. L. Xu *et al*., 3D multifunctional integumentary membranes for spatiotemporal cardiac measurements and stimulation across the entire epicardium. *Nat. Commun.* **5**, 3329 (2014).
18. J. Park *et al*., Electromechanical cardioplasty using a wrapped elasto-conductive epicardial mesh. *Sci. Transl. Med.* **8**, 344ra86 (2016).
19. S. Choi *et al*., Highly conductive, stretchable and biocompatible Ag–Au core–sheath nanowire composite for wearable and implantable bioelectronics. *Nat. Nanotechnol.* **13**, 1048–1056 (2018).
20. R. Arora *et al*., Arrhythmogenic substrate of the pulmonary veins assessed by high-resolution optical mapping. *Circulation* **107**, 1816–1821 (2003).
21. J. Kalifa *et al*., Mechanisms of wave fractionation at boundaries of high-frequency excitation in the posterior left atrium of the isolated sheep heart during atrial fibrillation. *Circulation* **113**, 626–633 (2006).
22. J. Christoph *et al*., Electromechanical vortex filaments during cardiac fibrillation. *Nature* **555**, 667–672 (2018).
23. I. R. Efimov, V. P. Nikolski, G. Salama, Optical imaging of the heart. *Circ. Res.* **95**, 21–33 (2004).
24. Y. Wang *et al*., A highly stretchable, transparent, and conductive polymer. *Sci. Adv.* **3**, e1602076 (2017).
25. Y. Liu *et al*., Soft and elastic hydrogel-based microelectronics for localized low-voltage neuromodulation. *Nat. Biomed. Eng.* **3**, 58–68 (2019).
26. B. Chu, W. Burnett, J. W. Chung, Z. Bao, Bring on the bodyNET. *Nature* **549**, 328–330 (2017).
27. T. Kazui *et al*., The impact of 6 weeks of atrial fibrillation on left atrial and ventricular structure and function. *J. Thorac. Cardiov. Sur.* **150**, 1602–1608 (2015).
28. L. Han *et al*., Mussel-inspired adhesive and tough hydrogel based on nanoclay confined dopamine polymerization. *ACS Nano* **11**, 2561–2574 (2017).
29. J. Liu *et al*., Syringe-injectable electronics. *Nat. Nanotechnol.* **10**, 629–636 (2015).
30. T. I. Kim *et al*., Injectable, cellular-scale optoelectronics with applications for wireless optogenetics. *Science* **340**, 211–216 (2013).
31. I. R. Minev *et al*., Biomaterials. Electronic dura mater for long-term multimodal neural interfaces. *Science* **347**, 159–163 (2015).
32. T. M. Fu *et al*., Stable long-term chronic brain mapping at the single-neuron level. *Nat. Methods* **13**, 875–882 (2016).
33. Z. Hu *et al*., Photochemically cross-linked perfluoropolyether-based elastomers: Synthesis, physical characterization, and biofouling evaluation. *Macromolecules* **42**, 6999–7007 (2009).
34. J. Y. Oh *et al*., Intrinsically stretchable and healable semiconducting polymer for organic transistors. *Nature* **539**, 411–415 (2016).